Biosensors and Bioelectronics 131 (2019) 250–256

Contents lists available at ScienceDirect

Biosensors and Bioelectronics

journal homepage: www.elsevier.com/locate/bios

Magnetic electrode-based electrochemical immunosensor using amorphous bimetallic sulfides of $CoSnS_x$ as signal amplifier for the NT−pro BNP detection

Yueyuan Li[a], Yaoguang Wang[a], Nuo Zhang[a], Dawei Fan[a], Lei Liu[a], Tao Yan[a], Xinglong Yang[a], Caifeng Ding[b], Qin Wei[a,*], Huangxian Ju[a,c]

[a] Key Laboratory of Interfacial Reaction & Sensing Analysis in Universities of Shandong, School of Chemistry and Chemical Engineering, University of Jinan, Jinan 250022, China

[b] Key Laboratory of Sensor Analysis of Tumor Marker, Ministry of Education, College of Chemistry and Molecular Engineering, Qingdao University of Science and Technology, Qingdao 266042, China

[c] State Key Laboratory of Analytical Chemistry for Life Science, Department of Chemistry, Nanjing University, Nanjing 210023, China

ARTICLE INFO

Keywords:
Amorphous bimetallic sulfides
$CoSnS_x$Pd
Magnetic glassy carbon electrode
NT–pro BNP
Immunosensor

ABSTRACT

In this work, by using amorphous bimetallic sulfides of $CoSnS_x$−Pd as signal amplifier and magnetic material of Fe_3O_4 @PPy−Au as the substrate, we fabricated an electrochemical immunoassay for N−terminal prohormone of brain natriuretic peptide (NT−pro BNP). $CoSnS_x$ was used as the signal amplifier of the immunosensor for the first time, which was synthesized by fast stoichiometric co-precipitation method. The binary sulfide was identified as an amorphous structure and performed apparent electrochemical behavior. The excellent performance of signal marker was induced by the synergistic effect between SnS_2 and cobalt, as well as the loaded Pd nanoparticles (NPs). Both $CoSnS_x$ and Pd NPs presented excellent electrocatalytic activity toward H_2O_2 oxidation. Moreover, the magnetic nanocomposite of Fe_3O_4 @PPy−Au was firmly immobilized on the magnetic glassy carbon electrode (MGCE) by the magnetic force. The magnetic substrate not only performed good electron conductivity, but also improved the stability of the fabricated electrochemical immunosensor. The developed immunosensor for the NT−pro BNP detection exhibited a wide linear response (0.1 pg/mL to 50 ng/mL), and low detection limit of 31.5 fg/mL. In addition, the immunosensor held an excellent analysis capability and broad fascinating application for the detection of other biomarkers in medical diagnosis and treatment.

1. Introduction

N−terminal prohormone of brain natriuretic peptide (NT−pro BNP) is a cardiac hormone prohormone, which is generated by heart muscle cells. And NT−pro BNP level in the blood is a hot topic in the field of cardiovascular diagnosis, because it is a good predictor of heart failure and indicates the left ventricular systolic function, the conditions of left ventricular diastolic dysfunction, balvular dysfunction and right ventricular dysfunction (Moses et al., 2011). At the same time, the investigators found NT−pro BNP level of patients with clinically diagnosed heart failure is higher than those without, which is 4639 pg/mL versus 108 pg/mL (Lin et al., 2014). Therefore, a novel method which can provide the wide detection range, high sensitivity and fast detection process is imperatively needed for the NT−pro BNP detection. The electrochemical immunosensor is one of the proper analysis measurements for the NT−pro BNP detection, and it is also a rapid, accurate and quantitative analysis method (Chunxiang et al., 2015; Li et al., 2015; Youxiu et al., 2015; Zhang et al., 2018). For these advantages, the electrochemical immunosensor have attracted researchers' significant attentions and been widely applied in the fields of drug screening, food inspection, environmental monitoring and clinical diagnosis (Qinfeng et al., 2013; Ren et al., 2017b, 2017c; Wang et al., 2018a; Zhan et al., 2018).

The non−enzymatic electrochemical immunosensor has been fabricated using metal oxides, metal sulfide, polymers, and metal−organic framework nanoparticles for the sensing of a target analyte (Ma et al., 2017; Peng et al., 2018; Ren et al., 2018a, 2017a; Zhang et al., 2017). Although lots of studies have been reported about the novel sensing material, the nanomaterial with the ability of fast response, excellent stability, low processing cost, easy synthesized and even high sensitivity

* Corresponding author.
E-mail address: sdjndxwq@163.com (Q. Wei).

https://doi.org/10.1016/j.bios.2019.02.007
Received 10 December 2018; Received in revised form 8 February 2019; Accepted 10 February 2019
Available online 21 February 2019
0956-5663/

for the immunosensor fabricated is still urgently needed. (Feng et al., 2015) Transition metal sulfides is a fascinating class among nano−⊜ materials, such as Cu_2S, CuS, CoS, SnS_2 and MoS_2, and has been extensively studied for its potential application in electrochemical immunosensor (Wang et al., 2015a, 2018b; Wei et al., 2018a). Moreover, the nanomaterial of SnS_2 has been well explored for its application in photovoltaics and optoelectronics (Wang et al., 2018a). Although the SnS_2 possesses good electrocatalytic activity toward H_2O_2 oxidation, its application in electrochemical immunosensor has been hindered by its poor electrical conductivity, especially when compared with other metal sulfides. Through adding cobalt into SnS_2 by fast stoichiometric co−precipitation, the $CoSnS_x$ is improved significantly in the electrical conductivity, and the electrochemical performance is promoted (Liu et al., 2017). At the same time, the $CoSnS_x$ not only retains excellent electrocatalytic activity of SnS_2 toward H_2O_2 oxidation of SnS_2, but also helps to develop synergistic effect between SnS_2 and cobalt to improve the electrocatalytic activity. Therefore, the $CoSnS_x$ is confirmed as an amorphous structure, which can provide more activity sites compared with crystalline forms of bimetallic sulfides (Ren et al., 2018b). In addition, the nanomaterial can serve as the buffer zone to mitigate the internal strain between each other (Wei et al., 2018a). In these conditions, the atomically mixed $CoSnS_x$ is advantageous over the mechanically mixed heterogeneous powders. Besides that, the $CoSnS_x$ can adsorb Pd (II) by electrostatic bonding and Pd NPs were loaded by the in-situ reduction method (Sun et al., 2013a). The introduction of Pd NPs not only improves the electron transport capacity and links the secondary antibodies (Ab_2) by Pd−N bond, but also enhances the catalytic property for H_2O_2 oxidation and increases the sensitivity of the immunosensor (Gao et al., 2018). In general, the $CoSnS_x$−Pd is a promising label for the fabrication of immunosensor.

Magnetic glassy carbon electrode (MGCE) is manufactured with a magnet, providing a stable strategy to immobilize the magnetic materials. The Fe_3O_4 can be firmly immobilized on the surface of MGCE by the magnetic force (Wang et al., 2015b). Polypyrrole (PPy) is one of electron conductive polymers, which not only improves the conductivity of Fe_3O_4 @PPy, but also links Au NPs by Au−N bond (Zhang et al., 2008). The magnetic nanocomposite of Fe_3O_4 @PPy−Au is a great substrate of immunosensor with MGCE, which not only has a good electron conductivity, but also improve the stability of the fabricated electrochemical immunosensor.

2. Material and methods

2.1. Synthesis of Fe_3O_4 @PPy−Au

Fe_3O_4 and Au NPs were synthesized according to the reports of Fang and Frens, respectively (Fang et al., 2017; Frens, 1973). And the preparation process of Fe_3O_4 and Au NPs were described in the Supporting Information.

Fe_3O_4 @PPy nanocomposite was prepared according to the report of Wang (Wang et al., 2012b). At first, 0.3 g of Fe_3O_4 was dispersed into 70 mL of water under sonication. Then, 15 mL of ethanol solution containing 3 mL of pyrrole and 10 mL of HCl (6 mol/L) were added into the above solution. The mixture was sonicated for 1.5 h. At last, the Fe_3O_4 @PPy was obtained after washing by ethanol and water.

For the preparation of Fe_3O_4 @PPy−Au, 1 mL of 10 mg/mL Fe_3O_4 @PPy was added into 40 mL of the prepared Au NPs solution. Followed by shaking for 5 h, the Fe_3O_4 @PPy−Au was gotten after magnetic separation and dried in the vacuum.

2.2. Synthesis of $CoSnS_x$−Pd

At first, the template of amorphous $CoSnS_x$, the single-crystalline $CoSn(OH)_6$ nanobox was prepared according to the report of Wang et al. (2013). At first, $SnCl_4$ (1 mmol, 5 mL) ethanol solution was added into 35 mL water solution which contained $CoCl_2$ (1 mmol) and sodium citrate (1 mmol) under stirring. Then 5 mL of 2 mol/L NaOH solution was added into the above solution dropwise. After stirring for 1 h, pink solid was obtained after washed by water and ethanol. The pink solid was dispersed into 40 mL of ultrapure water, and then 20 mL of 8 mol/L NaOH was added into the solution. After shaking for 15 min at room temperature, the color of the mixture changed to blue. At last, the pink $CoSn(OH)_6$ nanobox was obtained after washing with water and ethanol in turn for several times and dried in the vacuum.

The $CoSnS_x$ nanobox was synthesized according to the report of Liu et al. (2017) At first, 20 mg of $CoSn(OH)_6$ nanobox and 40 mg of thioacetamide were added into 30 mL ethanol and formed a uniform solution by ultrasonic dispersion. The mixture was transferred into a 50 mL of autoclave and heated at 140 °C for 12 h. After cooled to room temperature, the product was washed with water and ethanol by centrifugation. The $CoSnS_x$ nanobox was obtained after dried in vacuum.

The $CoSnS_x$−Pd was synthesized through the in-situ reduction method (Sun et al., 2013b). 60 mg of $CoSnS_x$ was dispersed in 80 mL of ethanol aqueous solution (50 vol%) in a 250 mL beaker, then the Na_2PdCl_4 (13 mL, 10 mmol/L) was added and mixed by ultrasonic. After that, excess $NaBH_4$ (0.2 mol/L) solution was dropwise added to the above mixture under stirring to reduce the metal ions for 2 h. At last, the $CoSnS_x$−Pd was obtained by centrifugation and dried in vacuum.

2.3. Preparation of the $CoSnS_x$−Pd−Ab_2

Fig. 1B shows the preparation process of the $CoSnS_x$−Pd−Ab_2. 1 mL of 10 μg/mL Ab_2 was added into 1 mL of 1.2 mg/mL $CoSnS_x$−Pd solution, and incubated for 12 h at 4 °C. After cryogenic centrifugation, the $CoSnS_x$−Pd−Ab_2 were obtained by dispersing in 1 mL of phosphate buffered solution (PBS, pH = 7.4) and maintained at 4 °C.

2.4. Fabrication of the immunosensor

Fig. 1 shows the fabrication process of the immunosensor. MGCE was polished by alumina powder and rinsed completely. Afterwards, 6 μL of 0.8 mg/mL Fe_3O_4 @PPy−Au solution was immobilized onto the surface of MGCE by the magnetic interaction between MGCE and Fe_3O_4 NPs. After drying, the Ab_1 (6 μL, 10 μg/mL) was modified on the electrode and incubated for 1 h, which can be linked by the widespread distribution of Au NPs. To eliminate the nonspecific binding sites of NT−pro BNP, 3 μL of 1 wt% BSA was modified on the electrode. After being washed thoroughly with PBS at pH = 7.4, various concentration of NT−pro BNP (6 μL, 0.1 pg/mL to 50 ng/mL) were modified on the MGCE. The MGCE was incubated for 1 h at room temperature and washed by PBS to remove the uncombined NT−pro BNP. Then, the solution of $CoSnS_x$−Pd−Ab_2 (6 μL, 1.2 mg/mL) was dropped on the MGCE and incubated for 1 h at room temperature. At last, the electrode was washed thoroughly by PBS again and stored at 4 °C when not being measured.

2.5. Experimental measurements

The fabricated immunosensor was analyzed by chronoamperometry. The electrode was tested in 10 mL of PBS (pH = 7.4) and the potential of the chronoamperometry was −0.4 V. After the signal background was at steady state, 10 μL of H_2O_2 (5 mol/L) was injected into PBS solution under mild stirring and the changed currents were recorded.

3. Results and discussion

3.1. Characterization of the applied nanomaterials

In this work, Fe_3O_4 @PPy−Au was used as the matrix of the immunosensor and characterized by the Fourier transform infrared

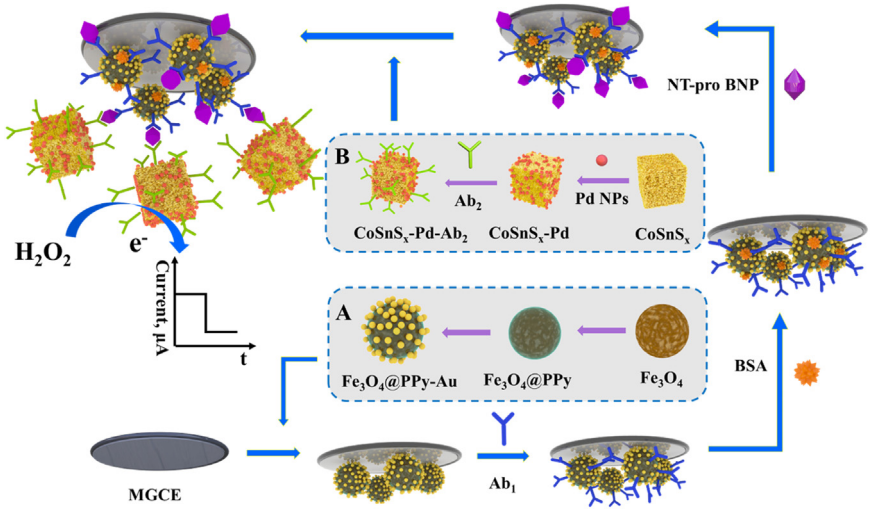

Fig. 1. The Schematic presentation of the fabrication of the immunosensor. The preparation process of Fe_3O_4 @PPy−Au (A) and $CoSnS_x$−Pd−Ab_2 (B).

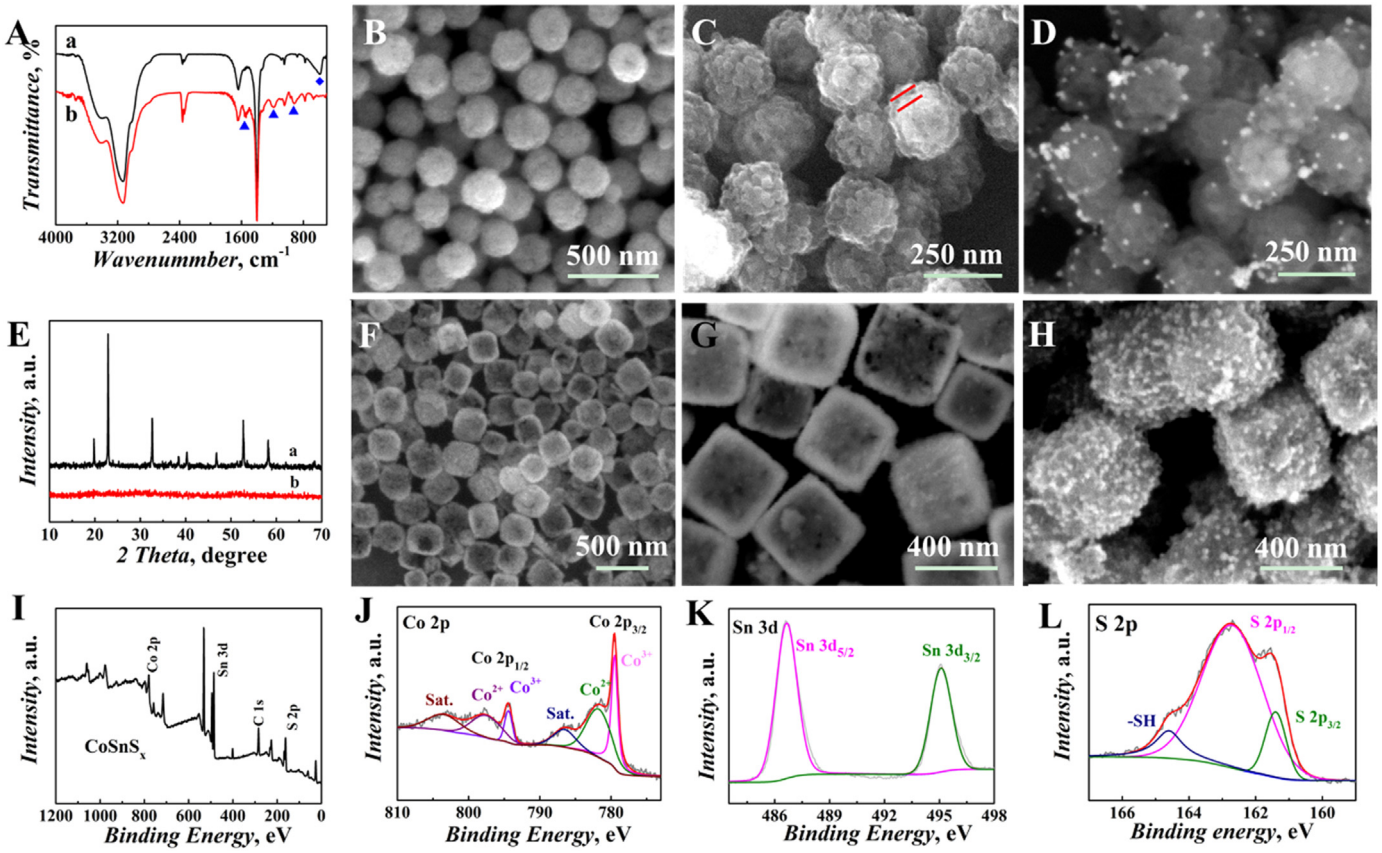

Fig. 2. (A) The FTIR spectrum of Fe_3O_4 (curve a) and Fe_3O_4 @PPy(curve b); the SEM images of Fe_3O_4 (B), Fe_3O_4 @PPy (C) and Fe_3O_4 @PPy−Au (D). The XRD (E) of the $CoSn(OH)_6$ (curve a) and $CoSnS_x$ (curve b); the SEM images of $CoSn(OH)_6$ (F), $CoSnS_x$ (G) and $CoSnS_x$−Pd (H); the XPS spectra of $CoSnS_x$ (I) in the Co 2p (J) and Sn 3d (K) and S 2p (L) regions.

spectroscopy (FTIR) spectrum, XRD and SEM methods. The FTIR spectrum of Fe_3O_4 and Fe_3O_4 @PPy were showed in Fig. 2A. The peak at 589 cm^{-1} (curve a) was the characteristic peak of Fe–O stretching, which revealed that Fe_3O_4 was prepared successfully (Ghosh et al., 2011). Compared with curve a, the new peaks appeared at around 1560 cm^{-1} (C=C stretching vibrations), 1185 cm^{-1} (C–N stretching vibrations), and 926 cm^{-1} (C–H out-of-plane vibrations) were observed from curve b (Wang et al., 2012a). These peaks corresponded to the characteristic peaks of PPy and the results clearly revealed that Fe_3O_4 @PPy composite was synthesized successfully. Meanwhile, the X−ray powder diffraction (XRD, Fig. S1) and the UV–vis adsorption results (Fig. S2) of Fe_3O_4, Fe_3O_4 @PPy and Fe_3O_4 @PPy−Au can be further verified that the Fe_3O_4 @PPy−Au was synthesized successfully. At the same time, the SEM images of Fe_3O_4 (Fig. 2B), Fe_3O_4 @PPy (Fig. 2C) and Fe_3O_4 @PPy−Au (Fig. 2D) were in accordance with the results of FITR spectrum, XRD and UV–vis adsorption.

The crystalline structure of $CoSn(OH)_6$ and $CoSnS_x$ were characterized with XRD. As shown in Fig. 2E, the main diffraction peaks at

2θ of 19.8°, 22.8°, 32.6°, 38.3°, 40.3°, 46.8°, 52.8°, 58.2° and 68.4° in $CoSn(OH)_6$ (curve a) can be found from perovskite-type $CoSn(OH)_6$ (JCPDS card No. 13–356) (Wang et al., 2013). There were no signals of $Co(OH)_2$ or SnO_2 which can be generated of the stoichiometrically controlled of Co^{2+} and Sn^{4+} in the presence of excess amount of OH^-. From the curve b, it can be seen that the signals from $CoSn(OH)_6$ phase disappeared totally, so it can be concluded that the structure of $CoSnS_x$ was amorphous. Meanwhile, the zeta potentials were detected and the value of $CoSn(OH)_6$ and $CoSnS_x$ were changed from + 34 mV to −16.1 mV. These results verified that the $CoSnS_x$ was synthesized successfully by the complete sulfidation of $CoSn(OH)_6$. The morphologies of $CoSn(OH)_6$ (Fig. 2F) and $CoSnS_x$ (Fig. 2G) demonstrated the nanobox observed from the SEM images. The morphology of the $CoSnS_x$ was consistent with the result of TEM (Fig. S3A). At the same time, the HRTEM (Fig. S3B) and the SAED (Fig. S3C) spectrum further indicated that the $CoSnS_x$ was amorphous structure. And the SEM of $CoSnS_x$—Pd (Fig. 2H) revealed that the Pd NPs were well scattered on the surface of $CoSnS_x$. Meanwhile, EDS of $CoSnS_x$—Pd in Fig. S4 can further prove that the Pd NPs was linked on the $CoSnS_x$ successfully. At the same time, the $CoSnS_x$ was determined by the EDS from TEM (Fig. S5 and Table S1), and the stoichiometry of $CoSnS_x$ is Co:Sn:S = 1:1:4. The co-existence of Co, Sn and S elements in $CoSnS_x$ nanobox was scanned by X—ray photoelectron spectroscopy (XPS), and the result was shown in Fig. 2I. The Co 2p spectrum was shown in Fig. 2J and divided into six peaks, which were assigned to $2p_{3/2}$ of Co^{3+} (779.5 eV) and Co^{2+} (781.9 eV), $2p_{1/2}$ of Co^{3+} (794.4 eV) and Co^{2+} (797.8 eV) and the corresponding satellite peaks (identified as “Sat.”) at 786.7 and 803.6 eV arise from Co^{2+} (Wei et al., 2018b). The Sn 3d spectrum was shown in Fig. 2K, and the presence of Sn^{4+} can be proved by the $3d_{5/2}$ (486.7 eV) and Sn $3d_{3/2}$ (495.1 eV) doublet (Wang et al., 2017). The S spectrum (Fig. 2L) can be separated into three different peaks, the peaks can be assigned to S $2p_{3/2}$ 1(61.4 eV) and S $2p_{1/2}$ (162.7 eV) and separated by a spin–orbit splitting of 1.3 eV (Zhang et al., 2006). Meanwhile, the S in thiol group peak appeared at 164.5 eV (Domazetis et al., 1979). From the results of XRD, SEM, EDS and XPS, it can be concluded that the $CoSnS_x$ and $CoSnS_x$—Pd were prepared successfully.

3.2. Electrochemical characterization of the immunosensor

To illustrate the electrochemical performance of matrix material (Fe_3O_4 @PPy—Au), the nanomaterial was characterized by square wave voltammetry (SWV). As shown in Fig. 3A, the oxidation peak current of the Fe_3O_4 (curve a) was small, after the PPy wrapped the Fe_3O_4 (Fe_3O_4 @PPy, curve b) and linked the Au NPs (Fe_3O_4 @PPy—Au, curve c), the oxidation peak current increased obviously. These results indicated that the PPy shell and Au NPs can improve the electron transfer ability, which can improve the sensitivity of the immunosensor. To explore the stability of magnetic materials immobilized on GCE and MGCE, the Fe_3O_4 @PPy—Au (0.8 mg/mL) was modified on the surface of the two type of electrodes. As shown in Fig. 3B and C, the samples of number 1 represented the bare GCE and MGCE signal responses and they were almost the same value to each other. The results implied that the sensitivities of GCE and MGCE were no obvious different with each other. The samples of number 2–4 were the modified electrodes submerged in the PBS for 0 min, 2 min and 5 min. We can find that the currents of the GCE decreased obviously and the MGCE were not. The results confirmed that the MGCE linked magnetic materials (Fe_3O_4 @PPy—Au) as the matrix can improve the stability of the immunosensor than GCE.

To confirm the signal amplification function of $CoSnS_x$—Pd in this work, the amperometric *i–t* measurement was utilized and the results were showed in Fig. 3D. The current response of CoS_2 (curve a) was smaller than SnS_2 (curve b), and the current response $CoSnS_x$ (curve c) was bigger than the both. The results indicated that the $CoSnS_x$ synthesized by fast stoichiometric co—precipitation method presented excellent electrocatalytic activity toward H_2O_2 oxidation. Furthermore, after loading Pd NPs, the current of $CoSnS_x$—Pd (curve d) was higher than $CoSnS_x$. These results indicated that the $CoSnS_x$—Pd was a good candidate as signal amplification. Furthermore, the CoS_2, SnS_2, $CoSnS_x$ and $CoSnS_x$—Pd were tested by SWV (Fig. S6). The results revealed that whether the addition of Co element to SnS_2 or the Pd NPs to $CoSnS_x$ can improve the electrical conductivity of $CoSnS_x$—Pd. Therefore, $CoSnS_x$—Pd was a good option to magnify the sensitivity of the immunosensor.

3.3. Electrochemical impedance spectroscopy (EIS) characterization of immunosensor

The Nyquist plots of the EIS for the modifying process was shown in Fig. 4A. It can be observed that bare MGCE exhibited a small resistance (curve a), and after the Fe_3O_4 @PPy—Au (cure b) modified on the MGCE, a bigger resistance was observed. After the surface of the electrode was blocked with Ab_1 (curve c), BSA (curve d), NT—pro BNP (curve e) and $CoSnS_x$—Pd—Ab_2 (curve f) by layer and layer method, the resistance values increased gradually and thee results revealed that the immunosensor was fabricated successfully.

3.4. Optimization of experimental conditions

To get the optimized conditions of the immunosensor and the best analytical performance of NT—pro BNP, the pH, concentrations of matrix (Fe_3O_4 @PPy—Au) and label ($CoSnS_x$—Pd—Ab_2) were chosen. The activity of the antibodies or antigens were affected by the pH. During the optimal experiment of pH, we used the same concentrations of Fe_3O_4 @PPy—Au (1.0 mg/mL) and NT—pro BNP (1.0 ng/mL) during the immunosensor fabrication. As shown in Fig. 4B, the best response signal appeared at pH = 7.4, and followed up these data we can get the optimum pH at 7.4. The concentration of the matrix (Fe_3O_4 @PPy—Au) was selected, and the results were showed in Fig. 4C. From these data, the optimal concentration of Fe_3O_4 @PPy—Au was chosen as 0.8 mg/mL. Subsequently, the optimal concentration of the signal label ($CoSnS_x$—Pd—Ab_2) of the immunosensor was detected and under 0.8 mg/mL of Fe_3O_4 @PPy—Au, 1.0 ng/mL NT-pro BNP and PBS with pH at 7.4 conditions. As shown in Fig. 4D, with the increase of the concentration of $CoSnS_x$—Pd—Ab_2, the signals increased from 0.4 mg/mL to 1.2 mg/mL and decreased from 1.2 mg/mL to 1.8 mg/mL. Therefore, the best concentration of $CoSnS_x$—Pd—Ab_2 was chosen at 1.2 mg/mL.

3.5. Assay performance

Under the optimal conditions, the record currents increase with the concentrations of NT—pro BNP (0.1 pg/mL ~ 50 ng/mL), and the responsed current were shown in Fig. 5A. The linear regression equations of the detection method was ΔI (μA) = 151.34 + 27.53 log$c$ (ng/mL, r = 0.996, Fig. 5B), and the limit of detection was 31.5 fg/mL (IUPAC, 2008). Compared to the reported work (Table S2), the proposed immunosensor exhibited a low limit of detection and wide linear range for NT—pro BNP detection. The developed technique present good analytical performance and application potential for other biomarkers which can be attributed to the following factors. Firstly, the matrix material of Fe_3O_4 @PPy-Au not only performed good electron conductivity, but also improved the stability of the fabricated immunosensor. Secondly, the signal amplifier label of $CoSnS_x$—Pd was a binary sulfide and identified as an amorphous structure, which performed apparent electrochemical behavior. Moreover, the $CoSnS_x$—Pd presented excellent electrocatalytic activity toward H_2O_2 oxidation due to the synergistic effect between SnS_2 and cobalt. Hence, the developed immunosensor can provide a stable immobilization and sensitivity detection method for the analogical biomarker detection and potential application in clinical sample.

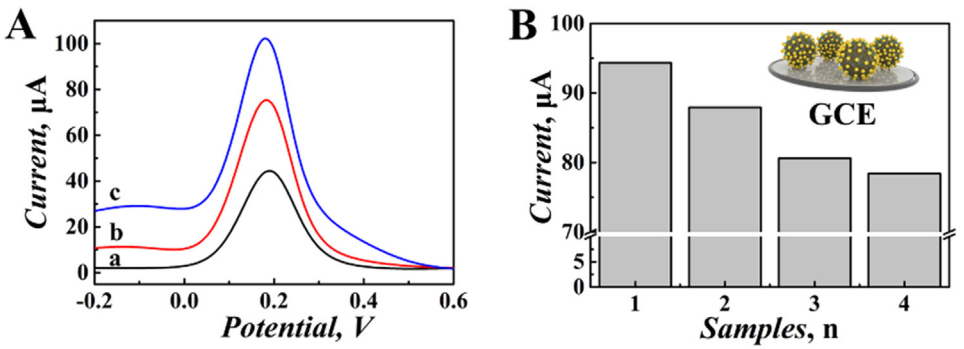

Fig. 3. (A) SWV response of the immunosensor with different labels: Fe_3O_4 (a), Fe_3O_4 @PPy (b) and Fe_3O_4 @PPy−Au (c). Oxidation peak current responses of GCE (B) and MGCE (C) modified without (1) and with 0.8 mg/mL of Fe_3O_4 @PPy−Au immersed in PBS for 0 min (2), 2 min (3) and 4 min (4). (D) Amperometric response of the immunosensors with different labels: CoS_2 (a), SnS_2 (b), $CoSnS_x$ (c) and $CoSnS_x$−Pd (d).

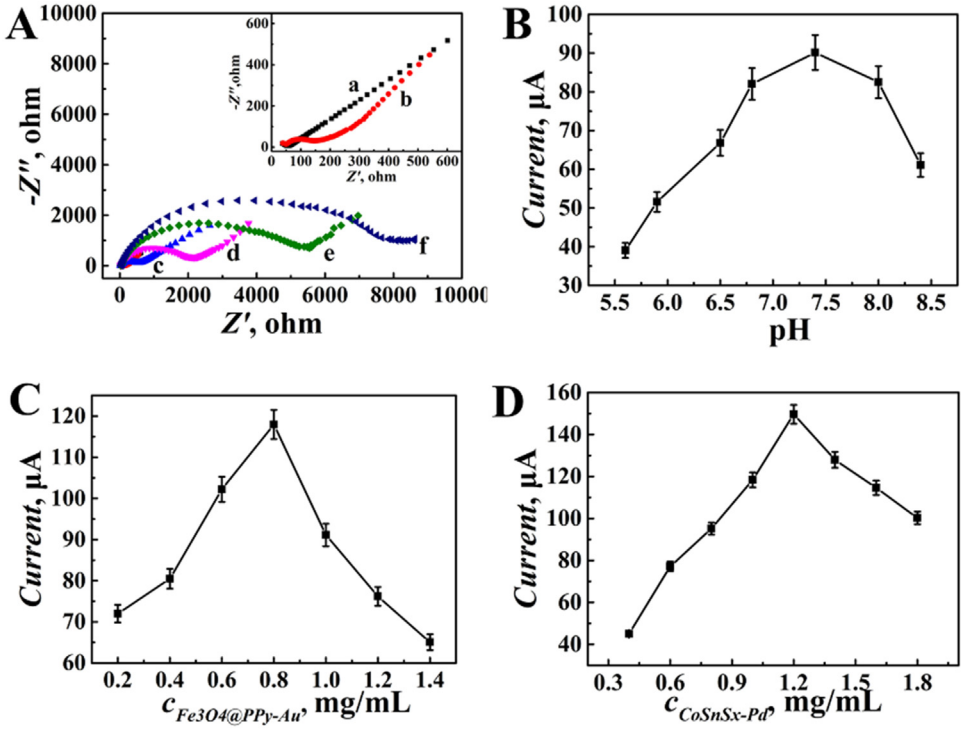

Fig. 4. (A) EIS obtained for different modified electrodes in $Fe(CN)_6^{3-/4-}$ containing 0.1 mmol/L KCl solution, MGCE (a), Fe_3O_4 @PPy−Au/MGCE (b), Ab_1/Fe_3O_4 @PPy−Au/MGCE (c), BSA/Ab_1/ Fe_3O_4 @PPy−Au/MGCE (d), NT−pro BNP/Ab_1/Fe_3O_4 @PPy−Au/MGCE (e) and $CoSnS_x$−Pd−Ab_2/NT−pro BNP/Ab_1/Fe_3O_4 @PPy−Au/MGCE (f). And the optimization of experimental conditions with (B) pH, (C) the concentration Fe_3O_4 @PPy−Au and (D) $CoSnS_x$−Pd−Ab_2 on the response of the immunosensor to 1.0 ng/mL insulin. Error bar = SD (n = 5).

3.6. Selectivity, reproducibility and stability

To demonstrate the potential of this immunosensor, the selectivity of the immunosensor was evaluated with interference substances, such as prostate−specific antigen (PSA), glucose, insulin and cyclic citrullinated peptide (CCP). As shown in Fig. 5C, the samples of numbers 1–4 just contained interference substances (10 ng/mL). The numbers 5–8 contained have 0.1 ng/mL of NT−pro BNP and 10 ng/mL of interference substances. The relative standard deviations (RSD) of the detection results were less than 5.0%, revealing that the method exhibited good selectivity. At the same time, the reproducibility of the fabricated immunosensor was conducted by detecting 10 pg/mL of NT−pro BNP sample. The results were shown in Fig. 5D, and the RSD of the detection method was less than 5.0%, which exhibited that the immunosensor presented a good reproducibility. The stability of the immunosensor was an important factor of the fabricated immunosensor (Wu et al., 2018). To further analysis the stability of this method, we fabricated the sensor and stored at 4 °C, the results were showed in Fig. S7. After ten days, there were no significant change of the signal response. And the response current decreased 4.3% when the

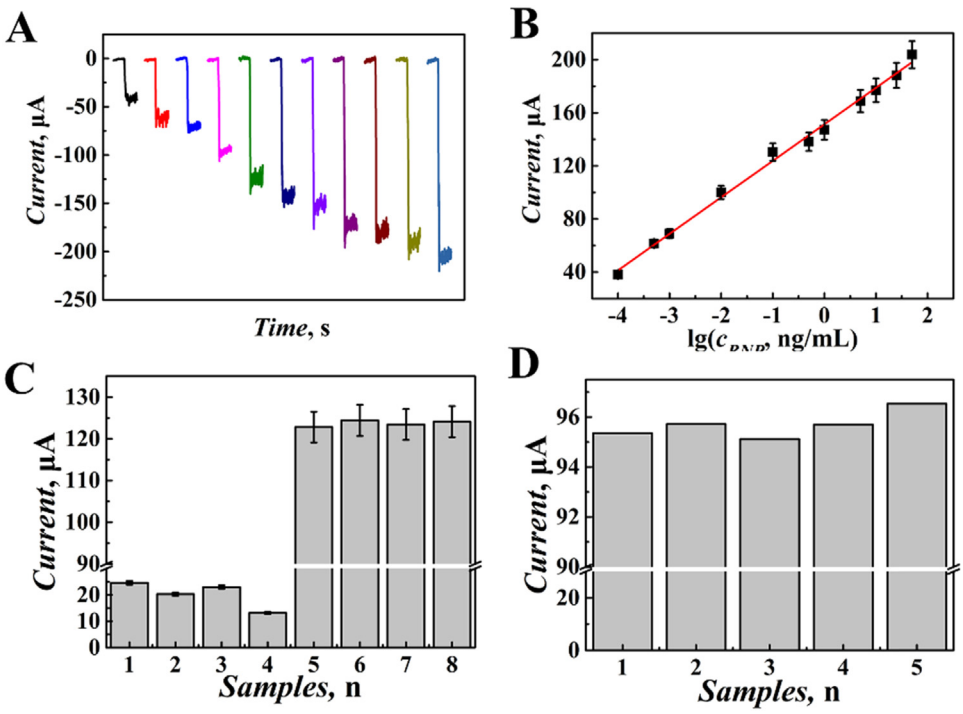

Fig. 5. (A) The current responses of the immunosensor (a~k: 0.0001 ng/mL, 0.0005 ng/mL, 0.001 ng/mL, 0.01 ng/mL, 0.1 ng/mL, 0,5 ng/mL, 1 ng/mL, 5 ng/mL, 10 ng/mL, 25 ng/mL and 50 ng/mL). (B) Calibration curve of the immunosensor toward different concentrations of NT−pro BNP. Figure 6. (C) The response of the immunosensor to 10 ng/mL PSA (1), 10 ng/mL glucose (2), 10 ng/mL insulin (3), 10 ng/mL CCP (4), 0.1 ng/mL NT−pro BNP + 10 ng/mL PSA (5), 0.1 ng/mL glucose + 10 ng/mL PSA (6), 0.1 ng/mL insulin + 10 ng/mL PSA (7) and 0.1 ng/mL CCP + 10 ng/mL PSA (8). (D) Current responses of five different electrodes for the reproducibility of 10 pg/mL of NT−pro BNP modified immunosensor. Error bar = SD (n = 5).

immunosensors were detected after one month. These data revealed that the novel immunosensor displayed receivable stability.

3.7. Real sample analysis

To further explore the adhibition of the immunosensor, a sample of healthy human serum was detected by the immunosensor and ELLSA method. The results were showed in Table S3, and the calculated values of *F−test* and *t−test* were F = 0.93 and t = 0.55 (df ≈ 10). The calculation formula of F and t were showed in Supplementary Information Table S3. These data suggested that there was no significant difference between the two detection methods and system error can be ignored. And the spike recovery test was tested by added different concentrations of NT−pro BNP (10 pg/mL, 50 pg/mL and 100 pg/mL) to the serum sample (Table 1). The recovery of detection NT−pro BNP by the fabricated immunosensor were in the range of 108.5~95.1% and the RSD were 4.16~4.94%. These data suggested that the immunosensor could be used in the clinically detection of NT−pro BNP in serum samples.

4. Conclusion

The sandwich-type immunosensor was fabricated for the NT−pro BNP detection by using amorphous bimetallic sulfides of $CoSnS_x$−Pd as signal amplifier and the magnetic material of Fe_3O_4 @PPy−Au as the matrix. The amorphous structure of $CoSnS_x$ presents excellent electrocatalytic activity toward H_2O_2 oxidation. And after the binary sulfides linked with Pd NPs, the detected signal can be improved significantly and get a sensitivity detection result. Moreover, the matrix of Fe_3O_4 @ PPy−Au can be firmly immobilized on the MGCE by the magnetic force and improve the stability of the immunosensor. The unique application of the bimetallic sulfides and magnetic material not only offers an easy, fast and high-accuracy analytical method, but also provides a promising way for clinical NT-pro BNP detection.

Table 1
The spike recovery test of the NT−pro BNP determination in serum sample.

Initial (pg/mL)	Added (pg/mL)	Found (pg/mL)	Average (pg/mL)	RSD (n = 5, %)	Recovery (%)
6.01	10	14.78, 16.40, 16.06, 15.48, 16.19	15.78	4.16	96.2
	50	56.68, 60.75, 57.22, 54.02, 53.95	56.52	4.94	108.5
	100	105.94, 112.52, 108.25, 102.55, 99.33	105.71	4.81	95.1

CRediT authorship contribution statement

Yueyuan Li: Conceptualization, Data curation, Writing - original draft. **Yaoguang Wang:** Methodology, Writing - review & editing. **Nuo Zhang:** Methodology, Writing - review & editing. **Dawei Fan:** Methodology, Writing - review & editing. **Lei Liu:** Formal analysis. **Tao Yan:** Methodology. **Xinglong Yang:** Investigation. **Caifeng Ding:** Writing - review & editing. **Qin Wei:** Funding acquisition, Project administration. **Huangxian Ju:** Funding acquisition, Project administration.

Acknowledgments

This work was supported by the National Key Scientific Instrument and Equipment Development Projects of China (No. 21627809, 21505051), and the National Natural Science Foundation of China (No. 21575050), and QW thanks the Special Foundation for Taishan Scholar Professorship of Shandong Province (No. ts20130937) and UJN.

Declaration of interests

None.

Appendix A. Supplementary material

Supplementary data associated with this article can be found in the online version at doi:10.1016/j.bios.2019.02.007.

References

Chunxiang, L., Hongyang, W., Jing, S., Bo, T., 2015. Anal. Chem. 87, 4283–4391.
Domazetis, G., Magee, R.J., James, B.D., 1979. J. Organomet. Chem. 173, 357–376.
Fang, Q.L., Duan, S.X., Zhang, J.F., Li, J.X., Leung, K.C.F., 2017. J. Mater. Chem. A 5, 2947–2958.
Feng, X., Tsz Wing, F., I-Ming, H., 2015. Acs Nano 9, 5027–5033.
Frens, 1973. Nature 241, 22.
Gao, Z., Li, Y., Zhang, C., Zhang, S., Li, F., Wang, P., Wang, H., Wei, Q., 2018. Biosens. Bioelectron. 126, 108–114.
Ghosh, S., Badruddoza, A., Uddin, M., Hidajat, K., 2011. J. Colloid Interfaces Sci. 354, 483–492.
IUPAC, 2008. Pure Appl. Chem. 33, 241–245.
Li, Z., Miao, X., Ke, X., Zhu, A., Ling, L., 2015. Biosens. Bioelectron. 74, 687–690.
Lin, D.C., Diamandis Jr, E.P., J.J., Maisel, A., Jaffe, A.S., Clerico, A., 2014. Clen Chem. 60, 1040–1046.
Liu, X., Wang, Y., Wang, Z., Zhou, T., Yu, M., Xiu, L., Qiu, J., 2017. J. Mater. Chem. A 5, 10398–10405.
Ma, H., Zhao, Y., Liu, Y., Zhang, Y., Wu, D., Li, H., Wei, Q., 2017. Anal. Chem. 89, 13049–13053.
Moses, E.J., Mokhtar, S.A.I., Hamzah, A., Abdullah, B.S., Yusoff, N.M., 2011. Lab. Med. 42, 75–80.
Peng, G., Li, X., Cui, F., Qiu, Q., Chen, X., Huang, H., 2018. ACS Appl. Mater. Interfaces 10, 17551–17559.
Qinfeng, X., Guichi, Z., Chun-Yang, Z., 2013. Anal. Chem. 85, 6915–6921.
Ren, X., Lu, P., Feng, R., Zhang, T., Zhang, Y., Wu, D., Wei, Q., 2018a. Talanta 188, 593–599.
Ren, X., Ma, H., Zhang, T., Zhang, Y., Yan, T., Du, B., Wei, Q., 2017a. ACS Appl. Mater. Interfaces 9, 37637–37644.
Ren, X., Wu, D., Ge, R., Sun, X., Ma, H., Yan, T., Zhang, Y., Du, B., Wei, Q., Chen, L., 2018b. Nano Res. 11, 2024–2033.
Ren, X., Yan, J., Wu, D., Wei, Q., Wan, Y., 2017b. ACS Sens. 2, 1267–1271.
Ren, X., Zhang, T., Wu, D., Yan, T., Pang, X., Du, B., Lou, W., Wei, Q., 2017c. Biosens. Bioelectron. 94, 694–700.
Sun, T., Zhang, Z., Xiao, J., Chen, C., Xiao, F., Wang, S., Liu, Y., 2013a. Sci. Rep. 3, 2527.
Sun, T., Zhang, Z., Xiao, J., Chen, C., Xiao, F., Wang, S., Liu, Y., 2013b. Sci. Rep. 3.
Wang, C., Tian, H., Jiang, J., Zhou, T., Zeng, Q., He, X., Huang, P., Yao, Y., 2017. ACS Appl. Mater. Interfaces 9, 26038–26044.
Wang, R., Wang, A.-J., Liu, W.-D., Yuan, P.-X., Xue, Y., Luo, X., Feng, J.-J., 2018a. Biosens. Bioelectron. 102, 276–281.
Wang, X., Chu, C., Shen, L., Deng, W., Yan, M., Ge, S., Yu, J., Song, X., 2015a. Sens Actuators B Chem. 206, 30–36.
Wang, Y., Fan, D., Zhao, G., Feng, J., Wei, D., Zhang, N., Cao, W., Du, B., Wei, Q., 2018a. Biosens. Bioelectron. 120, 1–7.
Wang, Y., Ma, H., Wang, X., Pang, X., Wu, D., Du, B., Wei, Q., 2015b. Biosens. Bioelectron. 74, 59–65.
Wang, Y., Zhao, G., Zhang, Y., Pang, X., Cao, W., Du, B., Wei, Q., 2018b. Sens Actuators B Chem. 266, 561–569.
Wang, Y., Zou, B., Gao, T., Wu, X., Lou, S., Zhou, S., 2012a. J. Mater. Chem. 22, 9034–9040.
Wang, Y.Q., Zou, B.F., Gao, T., Wu, X.P., Lou, S.Y., Zhou, S.M., 2012b. J. Mater. Chem. 22, 9034–9040.
Wang, Z., Wang, Z., Wu, H., Lou, X.W.D., 2013. Sci. Rep. 3, 1391.
Wei, Y., Ma, H., Ren, X., Ding, C., Wang, H., Sun, X., Du, B., Zhang, Y., Wei, Q., 2018a. Sens Actuators B Chem. 256, 504–511.
Wei, Y., Ren, X., Ma, H., Sun, X., Zhang, Y., Kuang, X., Yan, T., Ju, H., Wu, D., Wei, Q., 2018b. Chem. Commun. 54, 1533–1536.
Wu, D., Wei, Y., Ren, X., Ji, X., Liu, Y., Guo, X., Liu, Z., Asiri, A.M., Wei, Q., Sun, X., 2018. Adv. Mater. 30, 1705366.
Youxiu, L., Qian, Z., Yuping, L., Dianping, T., Reinhard, N., Dietmar, K., 2015. Anal. Chem. 87, 8531–8540.
Zhan, W., Chen, Z., Hu, J., Chen, X., 2018. Mater. Sci. Semicon. Proc. 85, 90–97.
Zhang, B., Ye, X., Dai, W., Hou, W., Xie, Y., 2006. Chemistry 12, 2337–2342.
Zhang, H., Zhong, X., Xu, J.-J., Chen, H.-Y., 2008. Langmuir 24, 13748–13752.
Zhang, L., Wang, Y., Shen, L., Yu, J., Ge, S., Yan, M., 2017. Analyst 142, 2587–2594.
Zhang, T., Ma, N., Ali, A., Wei, Q., Wu, D., Ren, X., 2018. Biosens. Bioelectron. 119, 176–181.